drones

MDPI

Article

Comparative Assessment of the Effect of Positioning Techniques and Ground Control Point Distribution Models on the Accuracy of UAV-Based Photogrammetric Production

Muhammed Enes Atik * and Mehmet Arkali

Department of Geomatics Engineering, Faculty of Civil Engineering, Istanbul Technical University, Istanbul 34469, Türkiye; markali@itu.edu.tr
* Correspondence: atikm@itu.edu.tr

Abstract: Unmanned aerial vehicle (UAV) systems have recently become essential for mapping, surveying, and three-dimensional (3D) modeling applications. These systems are capable of providing highly accurate products through integrated advanced technologies, including a digital camera, inertial measurement unit (IMU), and Global Navigation Satellite System (GNSS). UAVs are a cost-effective alternative to traditional aerial photogrammetry, and recent advancements demonstrate their effectiveness in many applications. In UAV-based photogrammetry, ground control points (GCPs) are utilized for georeferencing to enhance positioning precision. The distribution, number, and location of GCPs in the study area play a crucial role in determining the accuracy of photogrammetric products. This research evaluates the accuracy of positioning techniques for image acquisition for photogrammetric production and the effect of GCP distribution models. The camera position was determined using real-time kinematic (RTK), post-processed kinematic (PPK), and precise point positioning-ambiguity resolution (PPP-AR) techniques. In the criteria for determining the GCPs, six models were established within the İstanbul Technical University, Ayazaga Campus. To assess the accuracy of the points in these models, the horizontal, vertical, and 3D root mean square error (RMSE) values were calculated, holding the test points stationary in place. In the study, 2.5 cm horizontal RMSE and 3.0 cm vertical RMSE were obtained with the model containing five homogeneous GCPs by the indirect georeferencing method. The highest RMSE values of all three components in RTK, PPK, and PPP-AR methods were obtained without GCPs. For all six models, all techniques have an error value of sub-decimeter. The PPP-AR technique yields error values that are comparable to those of the other techniques. The PPP-AR appears to be an alternative to RTK and PPK, which usually require infrastructure, labor, and higher costs.

Keywords: photogrammetry; UAV; RTK; PPK; PPP-AR; Structure-from-Motion; GCP

Academic Editor: Pablo Rodríguez-Gonzálvez

Received: 4 December 2024
Revised: 20 December 2024
Accepted: 25 December 2024
Published: 27 December 2024

Citation: Atik, M.E.; Arkali, M. Comparative Assessment of the Effect of Positioning Techniques and Ground Control Point Distribution Models on the Accuracy of UAV-Based Photogrammetric Production. *Drones* **2025**, *9*, 15. https://doi.org/10.3390/drones9010015

1. Introduction

Unmanned aerial vehicles (UAVs) are widely used in various applications due to their capability to provide rapid and accurate mapping and generate three-dimensional spatial data. Especially, UAVs have become increasingly valuable in the domains of photogrammetry and remote sensing [1–4]. The quality of products such as orthophotos and digital elevation model (DEM) generated by UAVs is significantly enhanced with the integration of additional sensors, coupled with advancements in hardware and software technologies. Positioning is a fundamental component of spatial information in UAV photogrammetry, making the integration of Global Navigation Satellite System (GNSS)

receivers essential for maximizing operational effectiveness. In aerial photogrammetry, there are two approaches to georeferencing: direct and indirect [5–7]. Direct georeferencing determines the camera's position and orientation using onboard GNSS and IMU systems, removing the dependency on ground control points (GCPs). The indirect approach relies on GCPs, whose positions are known. It requires direct interaction with the surveyed area, careful GCP placement, precise image matching, and thorough calibration to ensure exact results.

In the absence of GCPs, the quality of GPS-based camera positions significantly affects the accuracy of UAV point clouds generated by direct georeferencing [8]. RTK necessitates the utilization of specific hardware and software components to attain high-precision positioning capabilities. The hardware includes a GNSS receiver that supports RTK functionality (compatible with GPS, GLONASS, Galileo, and BeiDou), an antenna (a high-quality unit designed to capture satellite signals with minimal interference and multipath errors), and a base station (a fixed reference point, or access to a network of reference stations with a known position, which requires an antenna and receiver that can transmit real-time correction data via RTK.). Data communication (transmitting real-time correction data from the base station to the rover receiver) is also essential. Software: includes components such as RTK processing, data recording, and analysis. In RTK mode, measurements are taken in real time, whereas in PPK mode, computations occur after the data are recorded [9]. The PPK method is applicable when there is a potential interruption with the base station during RTK measurement or when operating outside the coverage area, meaning no real-time corrections are available. PPK is regarded as a reliable and robust alternative to RTK. PPK is more flexible than RTK, allowing multiple types of data processing to minimize errors [10]. Furthermore, more accurate products (precise orbits, clock products, etc.) may enhance the processing methods. Relative positioning techniques require infrastructure, additional hardware (e.g., base GNSS station, RTK receiver), and more labor. These are aspects that restrict the study of UAV photogrammetry in some cases. Another alternative positioning technique to RTK and PPK is PPP. PPP technique based on absolute positioning is an alternative for UAV photogrammetry. The technique is straightforward and significantly reduces survey costs since users can collect data using a single GNSS receiver to determine their position. The PPP technique is an available solution in hard-to-reach areas where GCPs cannot be installed and require a GNSS infrastructure such as RTK/PPK. A dependable communications infrastructure is necessary for transmitting data to the rover's receiver; therefore, it makes the RTK approach challenging to utilize in places with insufficient communication, such as the polar areas [11]. The long convergence time has restricted the worldwide application of traditional PPP based on an ionosphere-free combination of dual-frequency observations [12]. The further shortcoming is that the large noise in the east component is probably a result of integer phase uncertainties that cannot be resolved for the PPP technique [13]. In the last decade, PPP with ambiguity resolution (PPP-AR) techniques have advanced from experimental to practical solutions [14]. PPP-AR improves the convergence time by shortening it and stabilizes the result in kinematic PPP research [15].

A comprehensive range of studies has been conducted to evaluate the precision of positioning in UAV photogrammetry [8–11]. These studies have revealed various findings on direct or indirect georeferencing. Current research is generally directed towards reducing dependence on GCPs. Determining the optimum GCP distribution and number is an important research area. Seo et al. [16] investigated the effect of GCP number and distribution on location accuracy in UAV-based orthophoto generation. Five scenarios were produced with four GCPs in the study. However, vertical accuracy was not included in the study. Zhao et al. [17] analyzed the impact of the number and distribution of GCPs on the

horizontal and vertical accuracy of photogrammetric products on glaciers. Different GCP distribution scenarios were used to optimize the models generated with PPK coordinates. Cho et al. [18] used the RTK-UAV to examine the accuracy decrease due to the lack of RTK signal in certain areas and mentioned that if one GCP is installed at the take-off point and post-process kinematic (PPK) is applied, in the case of a ground sampling distance (GSD) of about 3 cm, there may be an error level of H = 10 cm and Z = 20 cm up to a radius of 1 km. Elkhrachy et al. [19] investigated the accuracy improvement gained from using specific GCPs versus not employing any GCPs. The study by Erol et al. [20] searched to assess the effectiveness of real-time and post-processed GNSS kinematic point positioning techniques in UAV-based photogrammetric mapping accuracy. The effect of adjustment with GCPs was also examined. Tang et al. [21] intended to assess the effectiveness of UAV photogrammetry georeferencing in the absence of GCPs and to evaluate its feasibility for applications in the Antarctic region. Makineci et al. [22] introduced a novel methodology for positioning GCPs, focusing on the impact of the PPP technique on model accuracy, which significantly deviates from the current literature. Additionally, this research aims to assess how effective the PPP method is over different observation periods to determine the ideal duration for GNSS sessions. There are also studies comparing the effects of positioning techniques for UAV-based photogrammetry. Kim et al. [23] evaluated the geolocation accuracy of UAV mosaicked images of an abandoned mine by comparing orthomosaics and DEMs using standalone GNSS, differential GNSS, and PPP techniques. Martínez-Carricondo et al. [24] aimed to employ simultaneous differential corrections from several GNSS fixed base stations to increase the accuracy of UAV photogrammetry projects based on onboard GNSS RTK. Berber et al. [25] analyzed the data collected by UAVs in kinematic mode according to the PPP technique in open-source and web-based GNSS processing software and compared it with the results obtained from photogrammetric software. Gurturk et al. [26] compared the results of PPP-AR and PPK processing of the collected GNSS data in photogrammetric studies performed with two different flights. The 3D positioning analyses showed a difference distribution between 0 and 6 cm for both kinematic PPP and PPK results. Štroner et al. [27] showed a linear correlation between the computed internal orientation parameters (focal length) variance and the systematic height inaccuracy in models that only use onboard GNSS RTK data. Liu et al. [28] aim to evaluate the accuracy of UAV RTK/PPK direct georeferencing and the potential for rapid mapping in natural environments, including buildings and low vegetation. Ocalan et al. [15] investigated the performance of PPP and PPP-AR solutions derived from kinematic GNSS data obtained from UAVs by comparing them with PPP solutions based on relative positioning.

Based on these previous studies on GCPs, it is understood that the GCP distribution strategy is effective in improving localization accuracy in various mapping and surveying applications using aerial [16,17,29] or satellite imagery [30,31]. GCPs play an important role in minimizing errors originating from the GNSS receiver, topographic changes, and the sensor. Since marking a large number of GCPs requires high labor, cost-effective solutions need to be created to determine the appropriate distribution and number. On the other hand, further studies are needed to investigate the impact of GCP deployment on UAV-based photogrammetry applications in large urban areas.

This study investigates the integration of GCP distributions with different positioning techniques for UAV-based photogrammetry. It also investigates the accuracy of the RTK, PPK, and PPP-AR techniques in terms of producing orthomosaic and DEM. GCP distribution models were analyzed in the urban area based on six different scenarios. These three direct georeferencing methods are compared with the indirect georeferencing method. The contribution of the study is enhanced by the establishment of distribution models,

especially in urban areas, the comprehensive evaluation of the selection of appropriate GCPs, and the integration of precise positioning techniques and GCPs.

2. Materials and Methods

2.1. Structure-from-Motion

Structure-from-Motion (SfM) is a computer vision method that enables the calculation of 3D space coordinates from 2D images captured from different angles [32]. Conventional photogrammetry requires knowledge of the 3D position of a set of control points and external orientation elements (the coordinates of the image capture point and the rotation values of the image) to determine the 3D coordinates of points in a scene. On the other hand, the SfM approach does not require any of these to be known before the scene is reconstructed. Additionally, the camera pose and scene geometry are simultaneously reconstructed by automatically detecting similar features in various images.

The first step of the algorithm is the detection of matching points from multiple images by using feature extraction methods such as SIFT [33]. Feature-based methods have been widely used for the image matching step in SfM [34]. These methods are robust to homography transformations, perspective transformations, and illumination variations [35]. Matching features in two images are evaluated by the epipolar geometry, which is the intrinsic projective geometry between the two views. The epipolar geometry can be expressed using a 3×3 matrix which is known as the fundamental matrix (F).

$$x'Fx = 0 \tag{1}$$

where x' and x are the projected points of the 3D point onto the camera image plane [36].

To preliminarily calculate the fundamental matrix, matched features are used to apply the normalized eight-point algorithm. Thus, the coordinates of a 3D point in the scene can be calculated by triangulation with calibration, rotation, and translation matrices as follows:

$$\lambda_j \boldsymbol{x}_j = \mathbf{M}_j \boldsymbol{X}, j = 1, \cdots, n \tag{2}$$

where λ is a scale factor and $\mathbf{M}$ is the projection matrix, which is expressed as

$$\mathbf{M} = \begin{bmatrix} \mathbf{K} & 0 \end{bmatrix} \begin{bmatrix} \mathbf{R} & \boldsymbol{t} \\ 0^{\mathrm{T}} & 1 \end{bmatrix} \tag{3}$$

Bundle adjustment aims to iteratively minimize the distance between the projected and observed points. This method is used on the collective set of camera and scene parameters:

$$g(C, X) = \sum_{i=1}^{n} \sum_{j=1}^{m} \omega_{ij} \| \boldsymbol{x}_{ij} - \boldsymbol{P}(\boldsymbol{C}_i, \boldsymbol{X}_j) \|^2 \tag{4}$$

where ω_{ij} refers to an indicator variable: $\omega_{ij} = 1$ if camera i observes point j; otherwise, $\omega_{ij} = 0$; $\boldsymbol{C}$ is the collection of camera parameters for a single camera with $\boldsymbol{C}_i = \{\mathbf{M}, \mathrm{R}, t, k1, k2\}$; x_{ij} is the observed image point; and $\boldsymbol{P}(\boldsymbol{C}_i, \boldsymbol{X}_j)$ is the projected image point.

The objective function $g(C, X)$ is the sum of the quadratic projection errors. A sparse 3D point cloud is created at the end of this process [36].

The rotation and translation parameters expressed in Equations (2) and (3) can be obtained with high accuracy thanks to precise positioning techniques. The necessity of ground control points for the definition of 3D point clouds and other photogrammetric products in the scene in scale and reference coordinate system is decreasing.

2.2. Precise Point Positioning (PPP) Technique

The use of PPP in GNSS research is growing in interest since it has a high accuracy and the benefit of not needing base stations. The basis of the PPP technique was established with the publication by Anderle [37]. The first study on using PPP with GPS technology was conducted by Zumberge et al. in 1997 [38]. The PPP technique has been widely used in agriculture [39], seismic [40–42], structural health monitoring [43], atmospheric [44], and so on. The PPP technique is also used in areas where atmospheric and environmental conditions are challenging for studies, such as the polar regions [45]. Worldwide positioning is made possible by this technique, which does not require additional GNSS infrastructure (Figure 1). Utilizing a single receiver, the PPP technique uses single or multifrequency GNSS data to estimate 3D coordinates, precise satellite orbit, clock products, and code/phase biases in real-time or post-process.

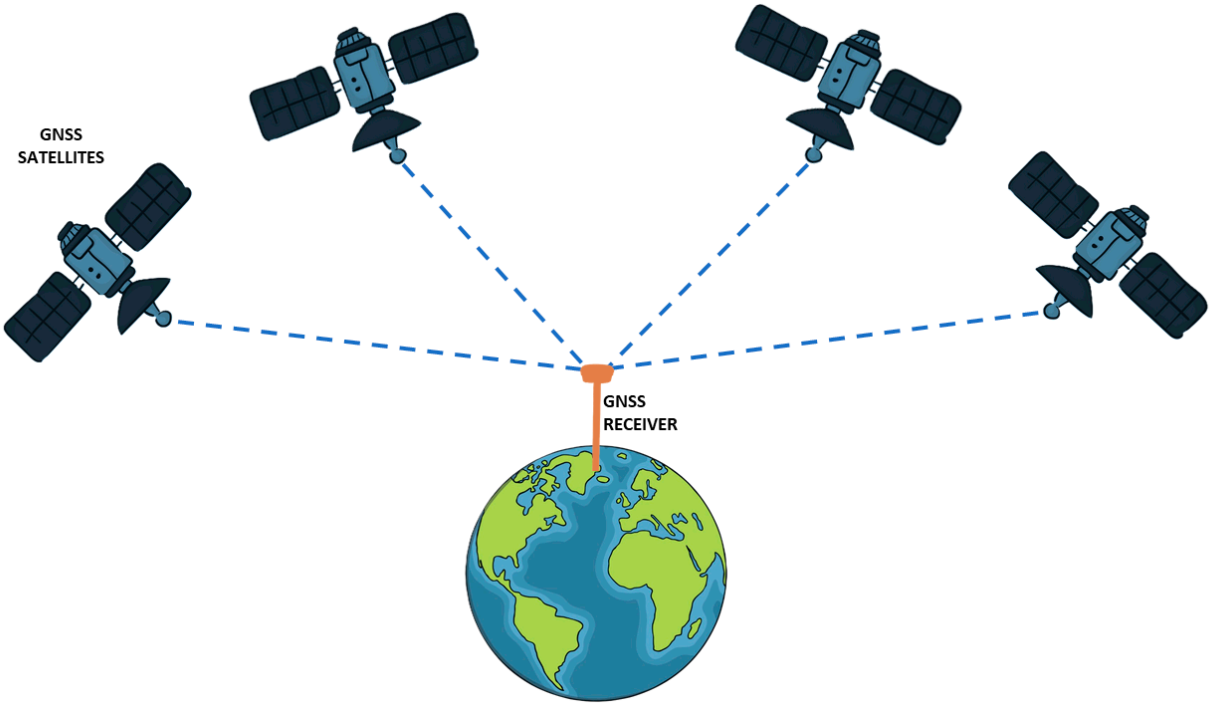

Figure 1. The basis of globally operating PPP.

The raw pseudo-range and carrier phase observation equations can be expressed as [46]

$$P^s_{r,f} = \rho^s_r + dt_r - dt^s + dT + a_f \cdot dI^s_{r,1} + D_{r,f} - D^s_f + \varepsilon_{P_f} \tag{5}$$

$$\Phi^s_{r,f} = \rho^s_r + dt_r - dt^s + dT - a_f \cdot dI^s_{r,1} + \lambda_f \left(N^s_{r,f} + B_{r,f} - B^s_f \right) + \varepsilon_{\Phi_f} \tag{6}$$

$$\rho^s_r = \sqrt{(x^s - x_r)^2 + (y^s - y_r)^2 + (z^s - z_r)^2} \tag{7}$$

where the subscript $f = (1,\ 2,\ 3, \cdots)$ relates to a specific carrier frequency, superscript s refers to satellites; ρ^s_r indicates the geometric distance between the satellite (x^s, y^s, z^s) and receiver (x_r, y_r, z_r); dt_r and dt^s are the clock errors of receiver and satellite; dT is the slant tropospheric delay; $dI^s_{r,1}$ is the slant ionospheric delay on the first carrier frequency and $a_f = \lambda^2_f / \lambda^2_1$ is the carrier frequency-dependent factor; $D_{r,f}$ and D^s_f are the receiver and satellite-specific code hardware delays; λ_f and $N^s_{r,f}$ are the wavelength in meter and integer ambiguity in cycle; $B_{r,f}$ and B^s_f are the receiver-dependent and satellite-dependent uncalibrated phase delays; ε_{P_f} and ε_{Φ_f} are the pseudo-range and carrier phase measurement noise, respectively [47].

The ionospheric-free combination is commonly employed in GNSS dual-frequency PPP in order to remove the impact of the first-order ionospheric delay.

$$\begin{aligned} P^s_{r,IF} &= \rho^s_r + dt_r - dt^s + dT + D_{r,IF} - D^s_{IF} + \varepsilon_{P_{IF}} \\ \Phi^s_{r,IF} &= \rho^s_r + dt_r - dt^s + dT + \lambda_{IF}\left(N^s_{r,IF} + B_{r,IF} - B^s_{IF}\right) + \varepsilon_{\Phi_{IF}} \end{aligned} \tag{8}$$

It is conventional to utilize precise orbit (x^s, y^s, z^s) and $\left(dt^s + D^s_{IF}\right)$ clock products from the IGS analysis center for the purpose of resolving satellite orbit and clock errors. Furthermore, the uncalibrated phase delays are inseparably associated with integer ambiguity. Equation (8) is consequently re-parameterized, and the error equation is expressed as follows:

$$\begin{aligned} r_{P_{IF}} &= \rho^s_r + \overline{d}t_r + \left(dt^s + D^s_{IF}\right) + dT - P^s_{r,IF} \\ r_{\Phi_{IF}} &= \rho^s_r + \overline{d}t_r + \left(dt^s + D^s_{IF}\right) + dT + \lambda_{IF}\overline{N}^s_{r,IF} - \Phi^s_{r,IF} \end{aligned} \tag{9}$$

Estimable parameters include receiver position (x_r, y_r, z_r), clock error $\overline{d}t_r$, tropospheric delay dT, and ambiguity $\overline{N}^s_{r,IF}$.

The term $\overline{N}^s_{r,IF}$ is usually decomposed to achieve PPP ambiguity resolution, i.e., to recover the integer property of ambiguity:

$$\overline{N}^s_{r,IF} = \left(\frac{cf_2}{f_1^2 - f_2^2} N^s_{r,WL} + \frac{c}{f_1 + f_2}\overline{N}^s_{r,NL}\right) / \lambda_{IF} \tag{10}$$

where $N^s_{r,WL}$ is the integer WL ambiguity and $\overline{N}^s_{r,NL}$ is the float NL ambiguity. Typically, the WL ambiguity is resolved by utilizing the Hatch–Melbourne–Wübbena (HMW) combination observable [48–50]. A tight constraint can be reconstructed and imposed on the ionosphere-free float ambiguities once the WL and NL integer ambiguities have been resolved and validated.

$$r_{N_{IF}} = \overline{N}^{s1}_r - \overline{N}^{s2}_r - N^{s1,s2}_r - d^{s1,s2} \tag{11}$$

In this form, PPP ambiguity resolution can be attained at the end-user level. Following the resolution of undifferenced ambiguities utilizing code and phase bias products, PPP may acquire a global positioning precision of millimeters, which aligns with traditional network analysis methods. The PPP-AR technique is more sensitive than the conventional PPP technique.

2.3. Real-Time Kinematic (RTK)

Following the late 1990s, RTK technology utilizing GNSS/GPS networks has emerged as the favored method globally. It is capable of achieving precision to within centimeters in a matter of seconds over distances of several kilometers. RTK surveying involves a base station transmitting raw GNSS data to rovers, which quickly computes a baseline between them, ideally within a few seconds (Figure 2). RTK accuracy mainly depends on the baseline length or the distance between the reference station and the rover. This is affected by orbital errors and atmospheric conditions. Radio waves or satellite communications are used to transmit the correction data [51].

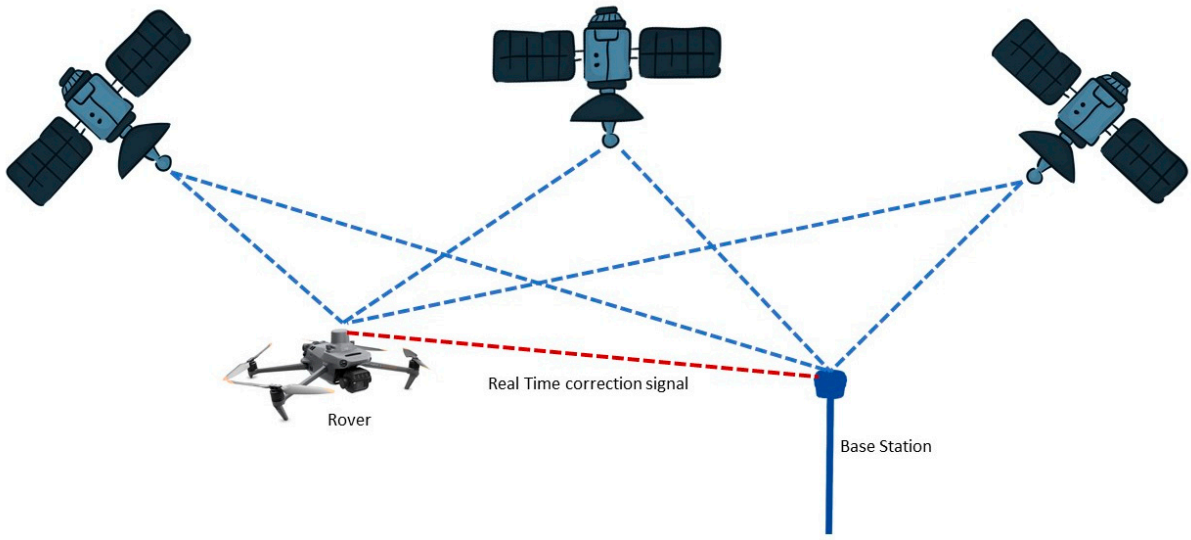

Figure 2. The fundamental concept of RTK GNSS positioning through the use of a UAV.

Consequently, the majority of prevalent errors can be mitigated through the application of differential techniques. Double differencing (DD) of carrier phase measurements is the basis of the RTK technique [52]. DD is utilized to eliminate errors from orbit, clock, and atmospheric delays while restoring the integer nature of phase ambiguities in carrier-phase observations.

While RTK GNSS positioning offers significant advantages, it is essential to acknowledge its practical limitations in real-world applications. RTK positioning is applicable only when a reference station is situated within a limited range, typically between 50 and 100 km. Furthermore, it necessitates substantial data flow channels to facilitate the transmission of correction signals. This situation results in extensive station maintenance and expensive costs.

2.4. Post-Processed Kinematic (PPK)

Post-processed kinematic (PPK) positioning is a relative positioning technique that is commonly employed in UAV-based photogrammetric projects. It makes use of the baseline solution post-field measurements. The PPK positioning technique commonly utilizes at least two GNSS receivers. In this configuration, the reference receiver, commonly called the base station, remains stationary on the ground, while the rover serves as the mobile receiver. To provide precise positional information, the PPK data are processed utilizing a reference station after the data have been collected. This processing method enhances the accuracy and reliability of the results obtained. Additionally, during the post-processing phase, precise ephemeris data for GNSS satellites are accessible, which often results in a more accurate solution. The PPK technique is applicable when the RINEX data are recorded during an active flight and are synchronized with data obtained from local receivers or the Continuously Operating Reference Station (CORS). Specifically, utilizing CORS data enables the execution of automated flight missions without the requirement of a base receiver or a connection to a network service for obtaining NRTK corrections [53].

2.5. Experimental Details

2.5.1. Study Area and Datasets

This research was conducted at the Ayazaga Campus of Istanbul Technical University in Türkiye (Figure 3). This campus features a mix of buildings, roads, and dense trees. The UAV-based photogrammetry flights covered an area of roughly 95 hectares.

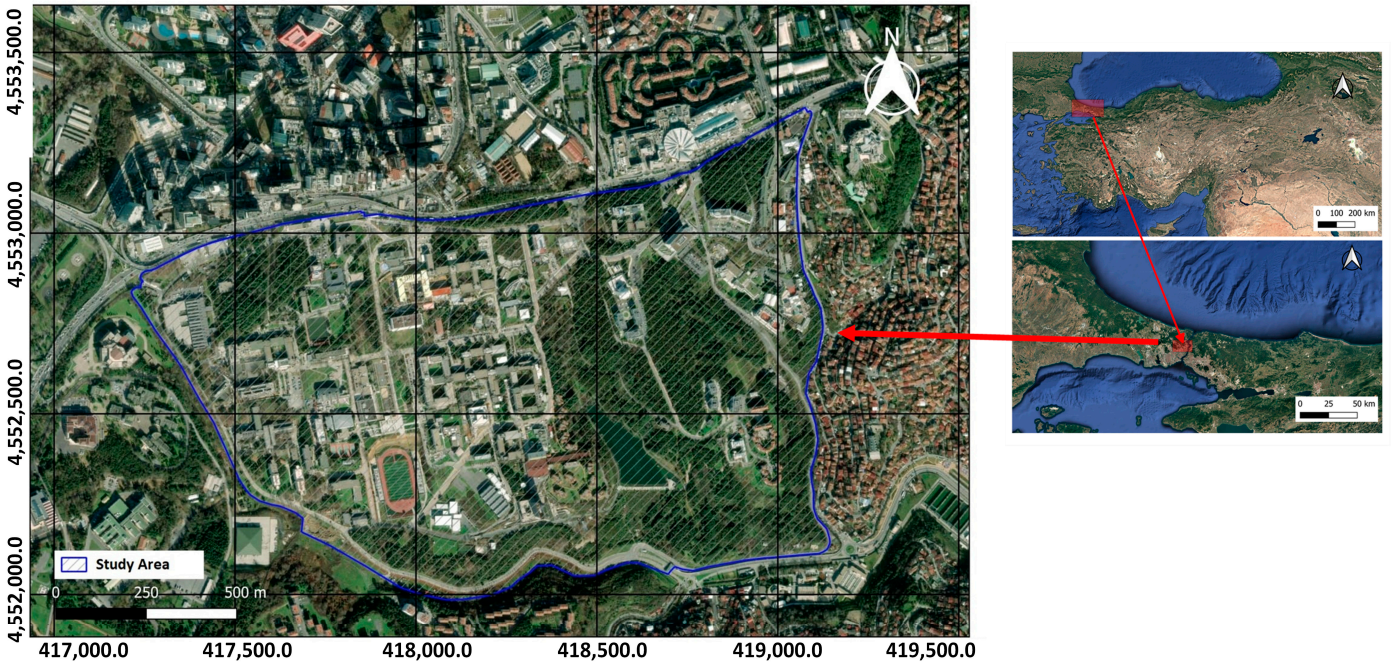

Figure 3. The study area is located on the Ayazaga Campus of Istanbul Technical University, Türkiye.

The research was carried out with the DJI Mavic 3M unmanned aerial vehicle (Table 1). The DJI Mavic 3M's lens features FOV: 84°, equivalent focal length: 24 mm, aperture: f/2.8 to f/11, focus: 1 m to ∞. The UAV collected images at an altitude of 60 m above the take-off point. Optimum flight parameters were determined as 80% longitudinal overlap ratio and 70% transverse overlap ratio. Therefore, around a 1.6 cm/pixel ground sampling distance (GSD) was obtained. The images were acquired from nadir angles. During the UAV flight, 2829 images in non-RTK mode and 3231 images in RTK mode were collected at 1 s intervals in the study area. The UAV's GNSS recorded data at 0.2-s (5 Hz) intervals.

Table 1. Features of UAV [54].

Equipment	Category	Feature
UAV	Model	DJI Mavic 3M
	Camera Sensor	20 Megapixels
	Max Flight Time (without wind)	43 min
	Max Takeoff Weight	1050 g
	Max Flight Speed (at sea level, no wind)	15 m/s (Normal Mode)
	GNSS	G + R [1] + E + C
	RTK Positioning Accuracy	RTK Fix: H: 1 cm + 1 ppm V: 1.5 cm + 1 ppm
	Operating Temperature	10° to 40° C (14° to 104° F)

[1] GLONASS is supported only when the RTK module is enabled.

2.5.2. Data Processing Steps and Analysis

In this study, UAV-based photogrammetry products were generated using indirect georeferencing, RTK, PPK, and PPP-AR techniques. Accuracy analyses were performed on 12 stable test points selected in the study area and six models with different point distributions. Test points were homogenously chosen from the study area (Figure 4).

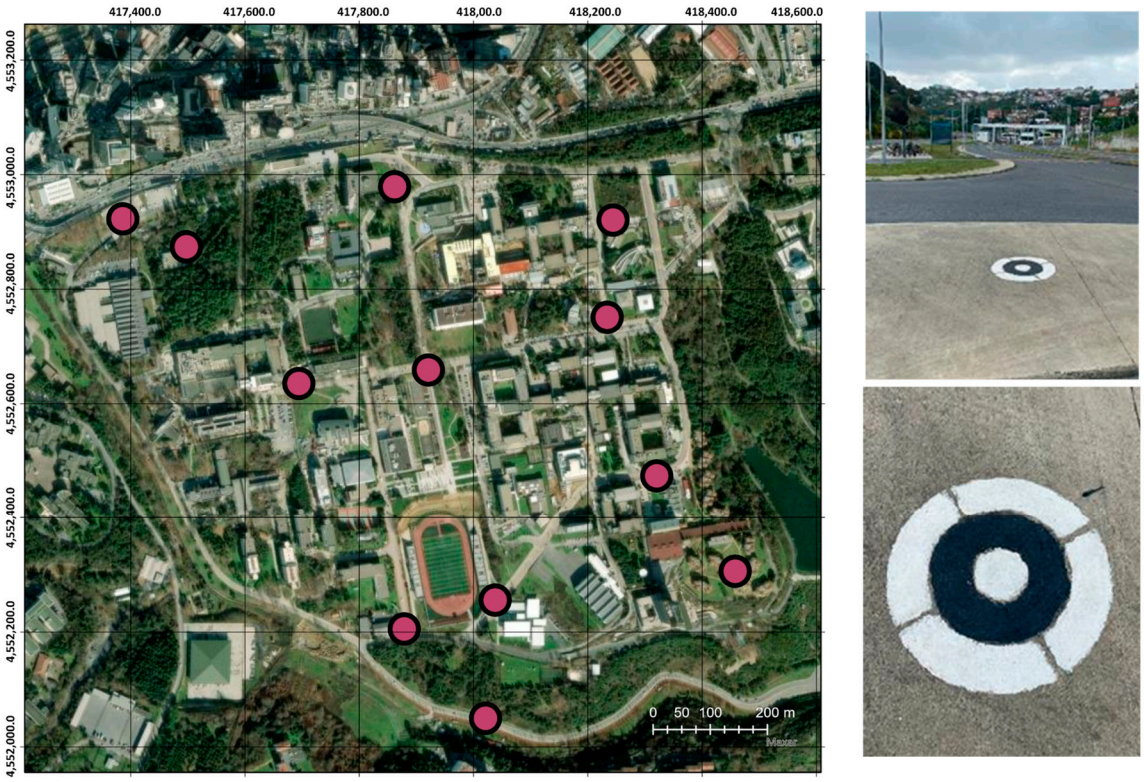

Figure 4. Distribution of test points (on **left**) in the study area and GCP sample (on **right**).

The GCPs used in the models are different from the test points. In this way, the same test points were used in each model (Figure 5). The models were created using 35 existing GCPs. Combinations and the number of points were selected according to criteria such as homogeneity, center, and edge. The accuracy of UAV-based photogrammetry was analyzed with different techniques with a total of 47 points, including check points (CPs) and GCPs. Model-1 is the model in which 35 GCPs are homogeneously distributed over the land. Model-2 contains 20 homogeneously distributed GCPs. Model-3 contains 5 homogeneously distributed GCPs. Model-4 includes 15 GCPs located at the edges of the study area. Model-5 includes 4 GCPs selected from the center of the study area in addition to Model-4. Model-6 consists of 4 GCPs located in the center of the study area.

The RINEX data collected in non-RTK mode were then analyzed using PPP-AR and PPK techniques. For RTK, it was connected to the ISKI-UKBS network (Figure 6). ISKI-UKBS network was accessed via mobile internet from the UAV console with a username and password. Real-time correction data were transmitted to the UAV through the network, allowing for the recording of precise coordinate data within the generated images. This enhances the accuracy of the position of the aerial imagery. PPK and PPP-AR techniques were used to obtain camera coordinates. Precise orbit and clock products improved the accuracy of the photogrammetric results. The workflow for both techniques is illustrated in Figure 7.

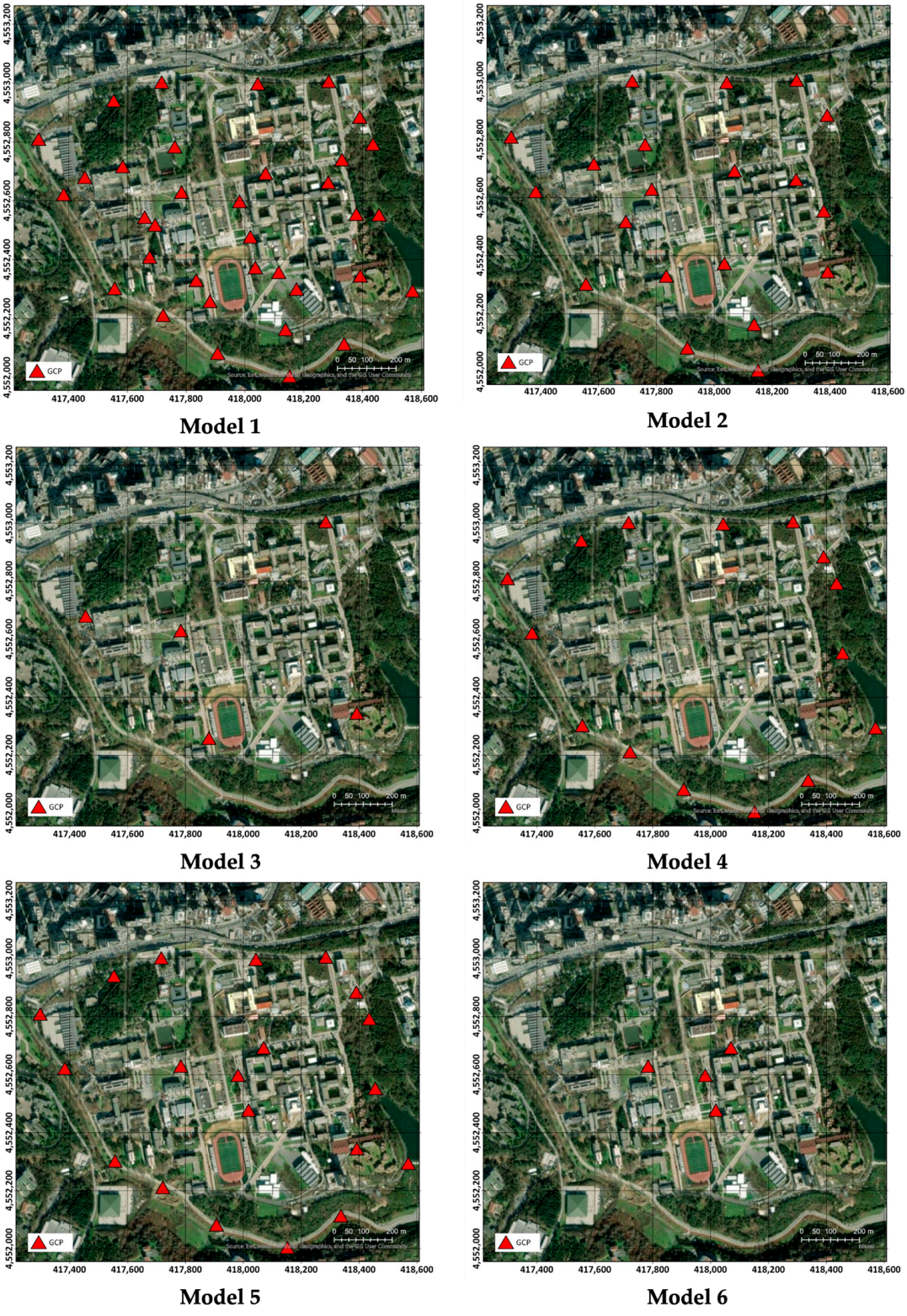

Figure 5. GCP distribution models generated in the study area.

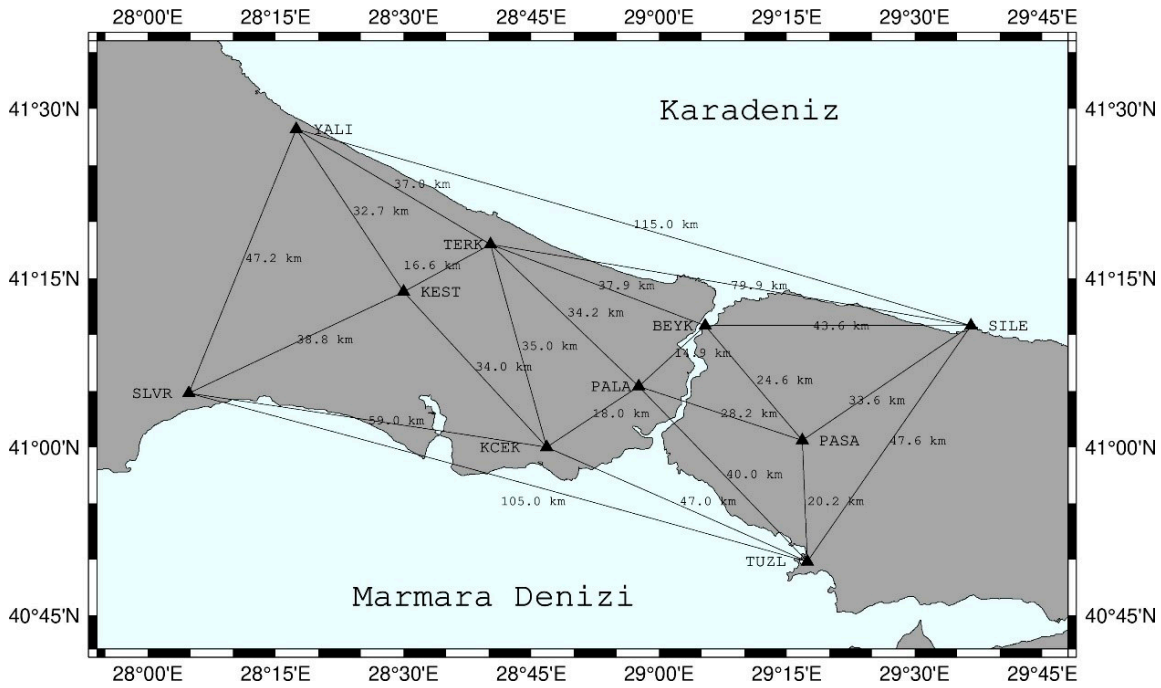

Figure 6. All stations of network ISKI-UKBS [55].

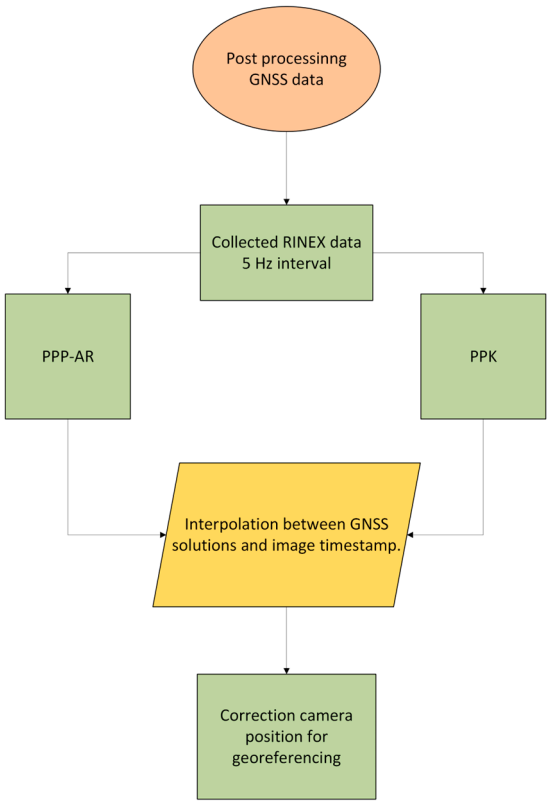

Figure 7. Workflow for post-processed positioning techniques.

PPK was employed to determine the camera positions based on the RINEX data obtained from the UAV. REDtoolbox software was used with a free trial version [56]. REDtoolbox provides a GNSS PPK processing solution when RTK is not available. The PALA station, part of the ISKI-UKBS network, served as the base station for this study (Figure 8). It is located approximately 5 km from the study area. The distance between the

base and the rover is within the suitable range for applying PPK. The solution focuses on determining the relative position between the base station and the UAV's GNSS.

In the following stage, camera positions were acquired utilizing the PPP-AR technique, which is based on absolute positioning. The technique was implemented using the open-source software PRIDE PPP-AR version 3.0.5 [57]. This software results from collaborative efforts by numerous GNSS experts at the GNSS Research Center at Wuhan University. RINEX data collected by the UAV were used during the experiment to investigate the PPP-AR solution's ability to correct the camera position. The PRIDE PPP-AR data processing strategy is summarized in Table 2. Kinematic processing was applied to acquire position information at each epoch. The coordinates obtained with PPP-AR were imported to the images according to the timestamp info.

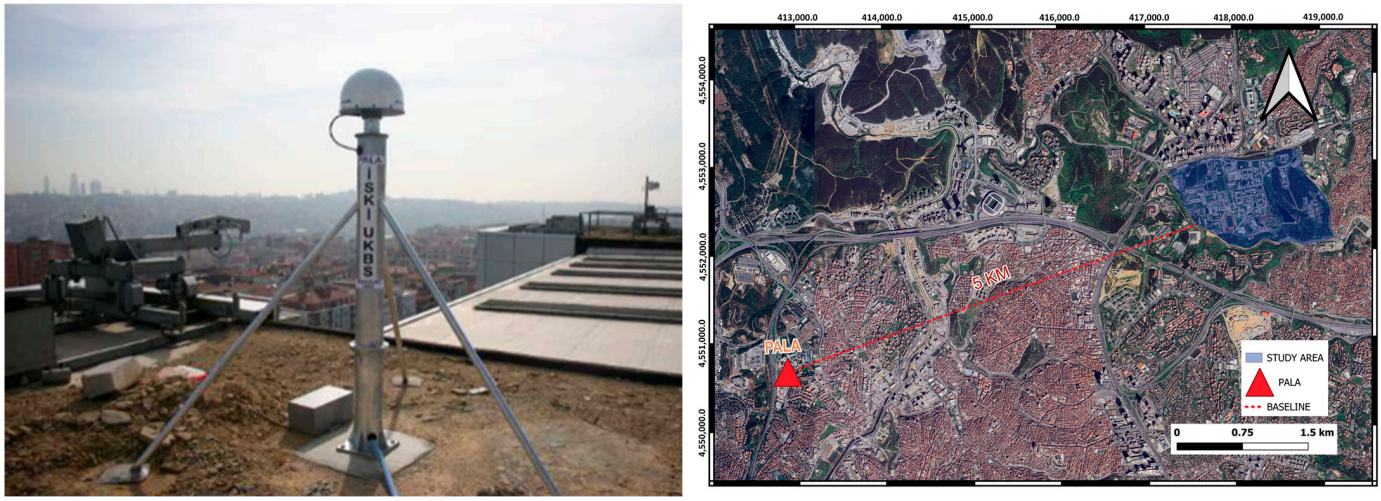

Figure 8. PALA station (on **left**) and distance (on **right**) from the study area.

Table 2. PRIDE PPP-AR processing parameters.

Item	Strategy
System	GNSS
Positioning Mode	Kinematic
Epoch Interval	0.2 s (5 Hz)
Cut Off Elevation Degree	7
Ambiguity Resolution	Fixed
Mapping Function	VMF3
2nd Ionospheric Delay Model	Yes
Ambiguity Fixing Method	LAMBDA
ZTD Model	STO
Receiver Clock Model	White Noise
HTG Model	NON
Strict Editing	Disable

In this study, the spatial accuracy of the solutions produced was determined by analyzing the differences between the measured coordinate and the model coordinates of the 12 CPs. The most common statistical method for determining accuracy is the root mean square error (RMSE) analysis. This method evaluates the difference between ground points with known coordinates (χ_G) and those obtained from the orthomosaic or 3D model (χ_M).

$$RMSE = \sqrt{\frac{\sum_{i=1}^{n} \left(\chi_{M_i} - \chi_{G_i}\right)^2}{n-1}} \quad (12)$$

Evaluations of the horizontal, vertical, and 3-dimensional accuracy of the georeferenced points were conducted for every positioning method and model.

3. Results

In this study, the effect of different positioning techniques on the accuracy of UAV-based photogrammetric products was compared. Different GCP distribution models were created using the GCP network created in Istanbul Technical University Ayazağa Campus. The effect of GCP distribution on the accuracy of UAV-based photogrammetry was investigated. Georeferenced orthomosaic and DEM were produced using the SfM algorithm with the DJI Terra software. There is no difference between the positioning techniques and GCP distribution models in terms of visualization of the final products. The obtained photogrammetric products are presented in Figure 9.

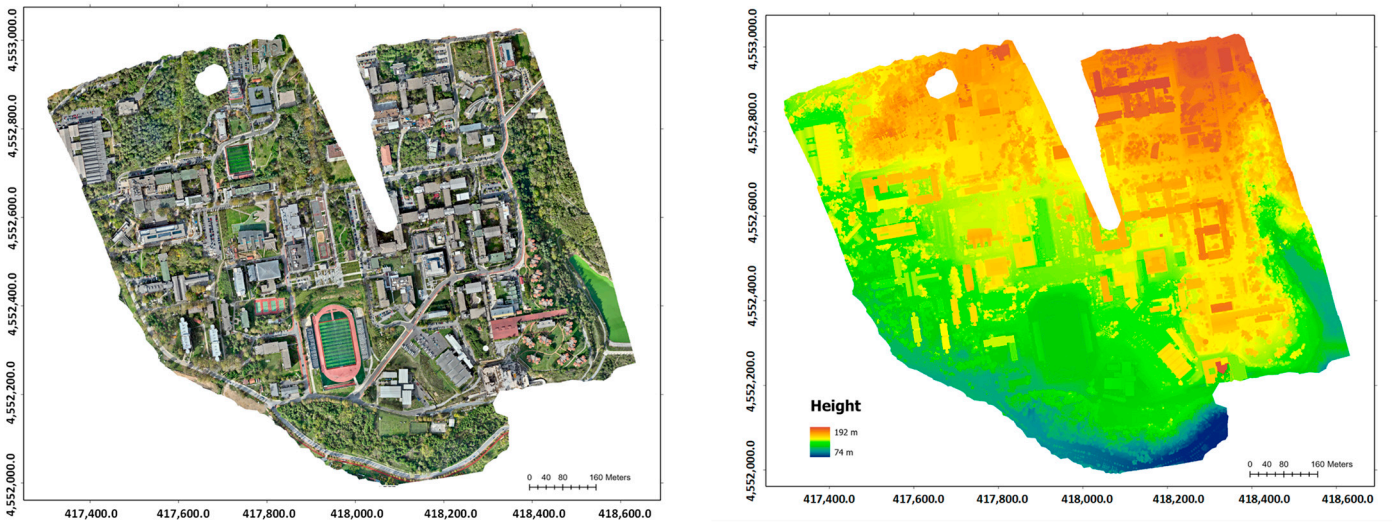

Figure 9. Orthomosaic (on **left**) and DEM (on **right**) produced as a result of photogrammetric evaluation.

RMSE values of different dispersion models are presented in Table 3. According to Table 3, 3D position accuracy improves significantly when GCP is added for RTK, PPK, PPP-AR. When the image coordinates obtained by RTK are balanced with the GCPs selected in Model-3, an RMSE of 1.4 cm is obtained. Vertical error is significantly reduced when GCP is added to all three methods. When applying indirect georeferencing, no results were produced without using GCP. This is because indirect georeferencing is a model that depends on GCPs measured with GNSS on the ground instead of the precise positioning module of the UAV. The impact of different GCP distribution models on accuracy is limited. With the RTK method, horizontal accuracy varies between 1.4–2.1 cm and vertical accuracy varies between 1.9–2.5 cm in all distribution models. The horizontal accuracy of the model generated with PPK is between 1.2–2.8 cm, and the vertical accuracy is between 1.3–1.9 cm. Similar to RTK, vertical accuracy increases significantly when GCP is used in the model generated with PPP-AR. Horizontal accuracy has values between 1.2–2.5 cm, and vertical accuracy is between 1.8–3.4 cm. The lowest horizontal RMSE was achieved using Model-3 in all techniques. Although there are similar numbers of GCPs in Model-6 to Model-3, only a small number of GCPs selected from the central region result in a lower horizontal accuracy than Model-3. Although Model-1 includes 35 points homogeneously distributed in the study area, similar RMSE values were obtained with other GCP distribution models.

Additionally, for each CP, the difference of the easting, northing, and height values from the reference values is presented with box plot graphs (Figure 10). Difference values

are generally normally distributed. In the RTK method, there are no outliers in both horizontal and vertical differences for all models. The median value for horizontal differences is around 2.5 cm for all models, while it varies between 4.5–6 cm for vertical differences. In the PPK method, there are outlier values in vertical differences in each distribution model. The median values of the vertical differences of the distribution models are around 3 cm. However, horizontal differences are gathered in a narrower range except for Model-5. There are no outliers in the horizontal differences, which are spread over a wide range in Model-1, Model-4, and Model-6. The lowest median value for horizontal differences was 1.9 cm in Model-4, while the highest median value was 3.15 cm in Model-6. The lowest horizontal difference value is 0.2 cm in Model-2, while the highest horizontal difference value is 5.6 cm in Model-4 and Model-5. The lowest vertical difference value is 0.1 cm in Model-2, and the highest vertical difference value is 8.5 cm in Model-4. When GCP is not used in the PPP-AR method, there are points with a vertical difference of more than 14 cm. The effect of Model-6 on vertical values is less than the other models. The lowest value in horizontal differences is 0.6 cm in Model-6, and the highest value is 4.8 cm in Model-1. The lowest values in the vertical difference were obtained in Model-1 and Model-2, which have homogeneous distributions. In Model-3, although the GCPs are homogeneously distributed, the vertical error is higher than the vertical error due to the low number of GCPs. In indirect georeferencing, the lowest median value in horizontal differences was obtained in Model-5 with 1.8 cm, while the highest median value was 2.35 cm in Model-6. There are outlier values in vertical differences in Model-1, Model-2, and Model-4. Model-5 and Model-6 are spread over a wider range than the other distribution models.

Table 3. RMSE values of CPs for each the positioning techniques based on the GCP distribution models. The unit of RMSE values is cm.

		No GCP	**Model-1**	**Model-2**	**Model-3**	**Model-4**	**Model-5**	**Model-6**
RTK	H	2.7	2.6	2.7	2.6	2.7	2.7	2.8
	V	8.1	4.5	4.8	6.5	6.8	6.2	7.1
	3D	8.5	5.2	5.5	7.0	7.3	6.7	7.7
PPK	H	2.9	2.9	2.8	2.7	2.9	3.0	3.0
	V	4.2	3.5	3.6	3.5	4.2	4.1	4.3
	3D	5.0	4.5	4.5	4.4	5.1	5.1	5.2
PPP-AR	H	2.9	2.9	2.9	2.8	2.7	2.9	3.1
	V	9.9	4.1	4.3	6.6	6.9	6.4	8.8
	3D	10.3	5.0	5.2	7.2	7.4	7.0	9.3
Indirect	H	-	2.9	2.8	2.5	3.0	3.0	2.7
	V	-	3.3	3.4	3.0	3.8	3.8	3.8
	3D	-	4.4	4.4	3.9	4.9	4.9	4.7

The graphs of the errors in X, Y, and Z directions according to the positioning technique for each CP are presented in Figures 11–13. X errors in the RTK method range from −3.3 cm to 3.2 cm. X errors in the RTK method range from −3.3 cm to 3.2 cm. The errors in the Y direction range between −4.5 cm and 4.4 cm. Generally, the points in the Y direction have fewer errors, although they are higher in some points. The errors in the Z direction are generally positive. The highest error was 13.9 cm without the use of GCP. In the PPK method, the errors in the X direction range from −3.9 cm to 3.3 cm. Errors in the Y direction range between −4.8 cm and 4.3 cm. The errors in the Z direction are between −8.5 cm and 8.5 cm. In the PPP-AR method, the errors in the Z direction are higher than X and Y. There are positive errors in the Z direction except for three GCPs. In the X direction, the errors vary between −3.6 cm and 3.5 cm, while in the Y direction, they vary between −4.6 cm and 4.1 cm. The highest absolute error is about 15 cm. In indirect georeferencing, the highest absolute error difference in the X coordinate is 4.2 cm. Errors in the Y direction were observed between −4.8 cm and 4.3 cm. In the Z coordinate direction, especially in

GCP-7, high errors were observed in models using many GCPs. Errors in the Z direction are between −9 cm and 7.5 cm.

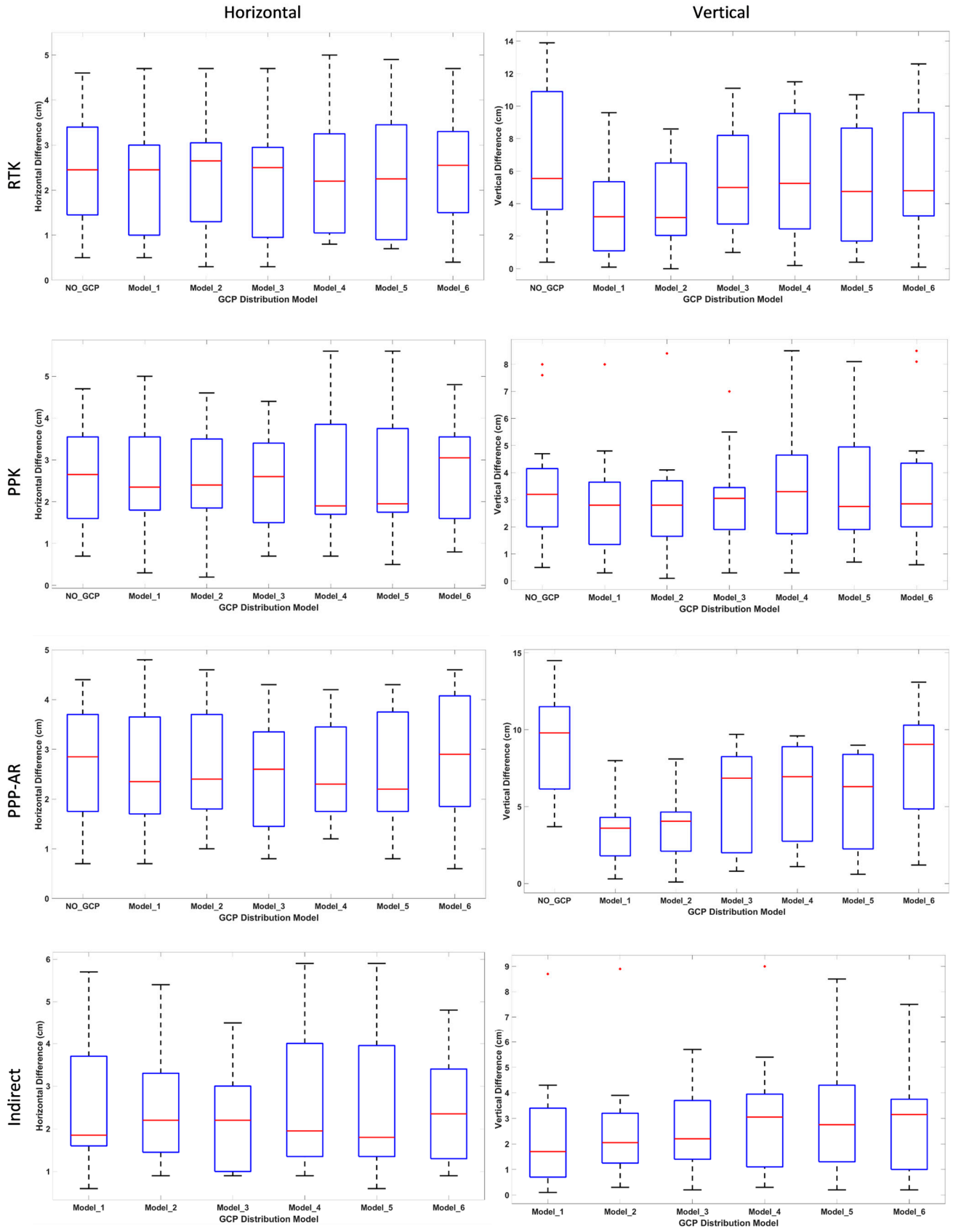

Figure 10. Box plot for horizontal and vertical differences in CPs. Red dots refer to outliers.

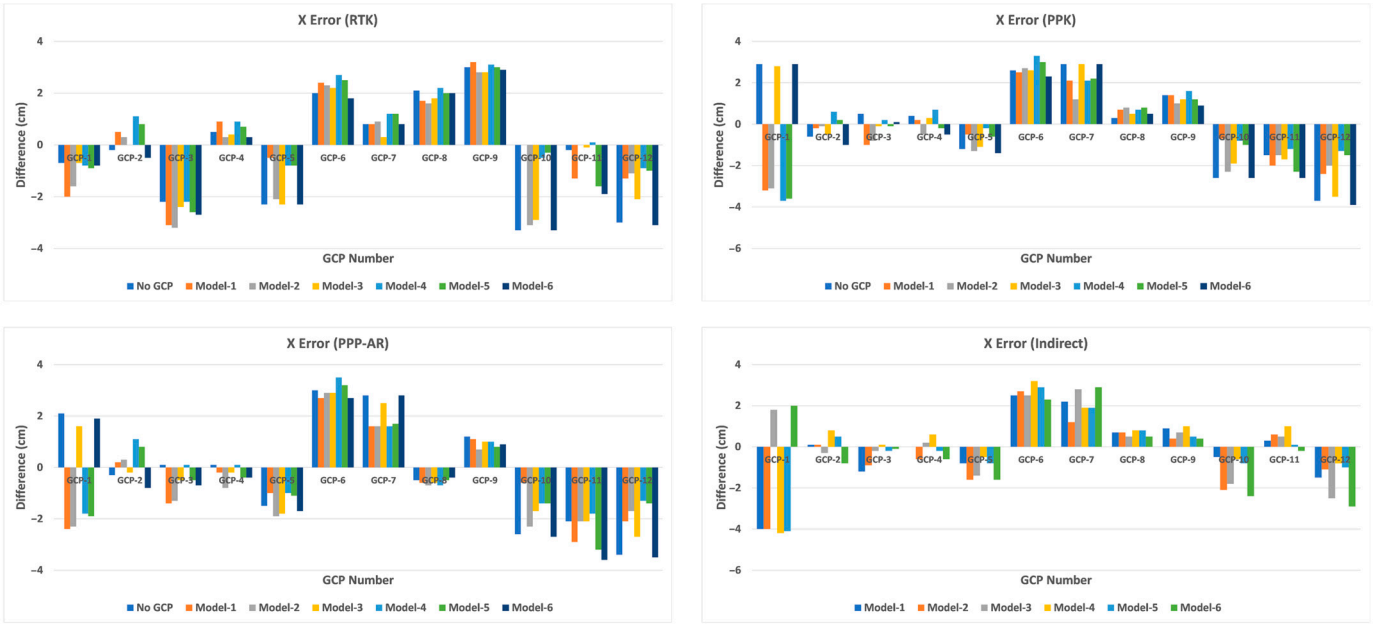

Figure 11. The errors in the X-axis were evaluated for each positioning technique.

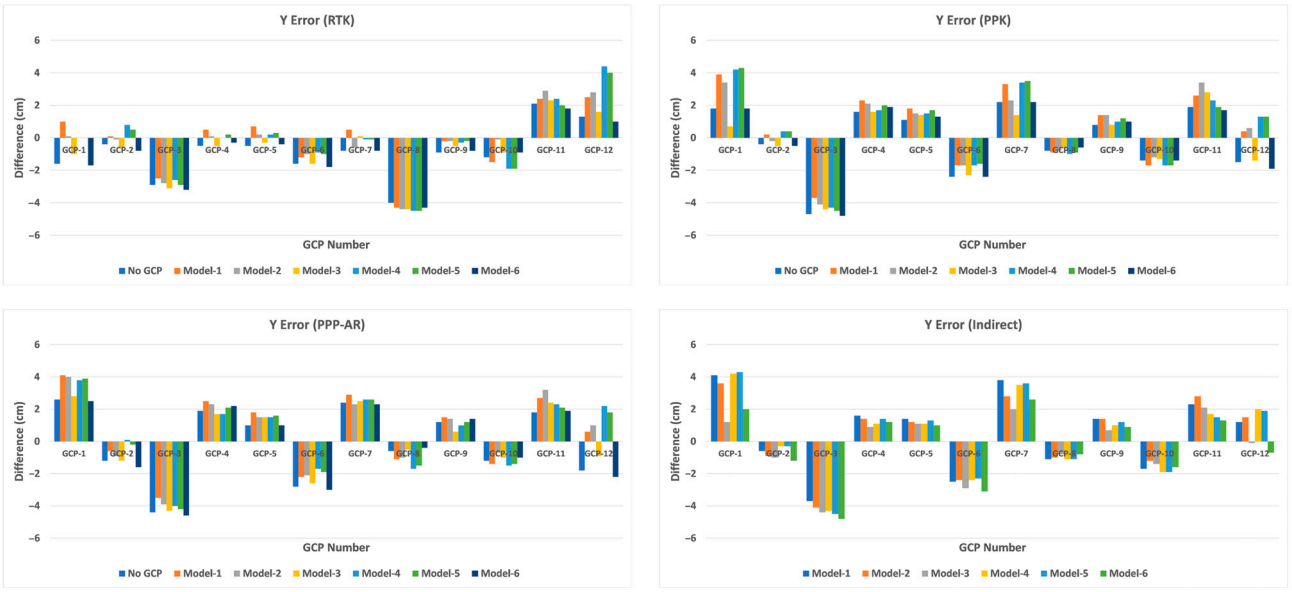

Figure 12. The errors in the Y-axis were evaluated for each positioning technique.

Figure 13. The errors in the Z-axis were evaluated for each positioning technique.

4. Discussion

In this study, projection center coordinates of the obtained aerial images were determined using RTK, PPK, and PPP-AR positioning techniques. Additionally, positioning techniques were integrated with different GCP distribution models to improve the accuracy of photogrammetric products. Four different methodologies were employed in the production of UAV-based photogrammetric products. The effectiveness of these methodologies was evaluated using models featuring GCPs that varied in distribution, location, and number. Furthermore, an analysis was conducted to assess the scenario in which no GCPs were utilized.

The methodology in this study proposes a more efficient approach in terms of GCP placement without reducing quality. Similar to the study by Seo et al. [16], our findings indicate that the placement of GCPs with the right strategy reduces the need for more GCPs and can be a cost-effective solution for UAV photogrammetric production. The results indicate that UAV-based photogrammetric products can be achieved with positioning accuracy at the centimeter level. An analysis of the error rates across horizontal, vertical, and 3D components demonstrates that the results from each technique exhibit close correspondence. According to the results, using a large number of GCPs does not guarantee higher accuracy. It is necessary to identify the most effective balance between the number and distribution of GCPs. Similar to other studies in the literature [20], vertical accuracies are significantly improved when GCPs are integrated with RTK, PPK, and PPP-AR methods. Although Model-1, Model-2, and Model-3 are homogeneously distributed, Model-3 contains fewer GCPs and thus has less effect on the vertical RMSE. The selection of the GCP distribution model slightly affects the horizontal RMSE values. Moreover, Model-6 does not include GCP from the edge regions which negatively affects the accuracy. For this reason, the RMSE values are reduced by including GCPs from the edge regions of the study region.

Direct georeferencing methods can reach centimeter level horizontal and vertical RMSE without the need for ground measurements. It is particularly suitable for photogrammetric mapping in inaccessible and disaster areas where it is not possible to install GCP. However, as reported in other studies, it gives lower accuracy to indirect georeferencing.

The data presented in Table 3 indicate that, when assessing all models, the indirect approach demonstrates the lowest error in the 3D components. Due to precisely located GCPs, the calculation of external orientation parameters with high accuracy is achieved

in the adjustment. According to the study results, indirect georeferencing using GCPs is a useful option that provides high accuracy. Moreover, since indirect georeferencing does not require precise positioning during flight, it is especially suitable for UAVs that do not contain an RTK module. On the other hand, its accuracy is dependent on GCP measurements and distribution and requires more field work.

According to Table 3, it has been observed that PPK demonstrates greater accuracy in the vertical component across all evaluated models compared to RTK. Conversely, for the accuracy in the horizontal component in all models, RTK exhibits superior performance compared to PPK. For the 3D component, PPK has better performance compared to RTK in all models, including those without GCPs. The reason for the better performance of PPK may be that the correction data may not be received continuously during the RTK procedure due to internet interruptions. Using precise orbits and clock products is another reason for improving the PPK results.

Analysis of the absolute positioning-based PPP-AR technique in all models shows that the error remains at the centimeter level in all three components. PPP-AR achieved a similar precision level to that of the relative techniques. The open-source software PRIDE PPP-AR improves the PPP technique with ambiguity resolution thanks to the algorithm it runs in the background. It has been found that PRIDE PPP-AR software performs better compared to services with similar PPP techniques [58]. In this study, the PPP-AR technique was considered an alternative to RTK/PPK techniques, which require more infrastructure, labor, and cost. The analysis of the horizontal, vertical, and 3D components indicates that the results of the PPP-AR technique are consistent with those of the alternative techniques. Since RTK requires an instant mobile connection due to its structure, it may have a negative effect in case of signal failure. The accuracy will not reach the desired level because the correction data cannot be received in real time. Furthermore, an additional GNSS for RTK/PPK adds an extra workload.

5. Conclusions

This study involved the development of six distribution models utilizing GCPs in conjunction with various positioning techniques to evaluate the accuracy of photogrammetric products. The focus was on assessing each CP's horizontal, vertical, and three-dimensional position components. A thorough analysis considered several factors, including the number of points, their locations, and the overall distribution of these points within the area. This examination offered results into the influence of these factors on the accuracy and reliability of the resulting photogrammetric outputs.

It may not be possible to establish a GCP in certain parts of the study area due to various factors. These factors include locations that pose difficulties in terms of accessibility, areas considered hazardous, and areas where access is restricted or prohibited. In areas with numerous settlements, the establishment of GCPs may face difficulties in terms of permanence and visibility. For this reason, the use of precise positioning techniques for UAV-based photogrammetric assessment provides wide benefits. Promising results can be obtained using the appropriate method. However, this does not make GCPs completely unnecessary. The use of GCPs in an appropriate number and distribution contributes particularly to improving vertical accuracy.

With the development of satellite technologies, different positioning systems are being developed by countries. In future studies, it is planned to examine the effects of different satellite systems on UAV-based photogrammetry individually. Moreover, future research could further optimize the GCP distribution strategy by considering several factors, such as terrain characteristics, camera angle, flight altitude, and ground sampling distance.

Author Contributions: Conceptualization, M.E.A. and M.A.; methodology, M.E.A. and M.A.; software, M.E.A. and M.A.; validation, M.E.A.; formal analysis, M.A.; investigation, M.A.; resources, M.E.A.; data curation, M.E.A.; writing—original draft preparation, M.E.A. and M.A.; writing—review and editing, M.E.A.; visualization, M.E.A. and M.A.; supervision, M.E.A. All authors have read and agreed to the published version of the manuscript.

Funding: This research was funded by the Istanbul Technical University Scientific Research Projects Office (BAP), grant number MGA-2023-44835.

Institutional Review Board Statement: Not applicable.

Informed Consent Statement: Not applicable.

Data Availability Statement: The original contributions presented in this study are included in the article. Further inquiries can be directed to the corresponding author(s).

Conflicts of Interest: The authors declare no conflicts of interest.

References

1. Feng, Q.; Liu, J.; Gong, J. UAV Remote Sensing for Urban Vegetation Mapping Using Random Forest and Texture Analysis. *Remote Sens.* **2015**, *7*, 1074–1094. [CrossRef]
2. Fraser, R.H.; Olthof, I.; Lantz, T.C.; Schmitt, C. UAV Photogrammetry for Mapping Vegetation in the Low-Arctic. *Arct. Sci.* **2016**, *2*, 79–102. [CrossRef]
3. Šašak, J.; Gallay, M.; Kaňuk, J.; Hofierka, J.; Minár, J. Combined Use of Terrestrial Laser Scanning and UAV Photogrammetry in Mapping Alpine Terrain. *Remote Sens.* **2019**, *11*, 2154. [CrossRef]
4. Liu, J.; Xu, W.; Guo, B.; Zhou, G.; Zhu, H. Accurate Mapping Method for UAV Photogrammetry Without Ground Control Points in the Map Projection Frame. *IEEE Trans. Geosci. Remote Sens.* **2021**, *59*, 9673–9681. [CrossRef]
5. Shahbazi, M.; Sohn, G.; Théau, J.; Menard, P. Development and Evaluation of a UAV-Photogrammetry System for Precise 3D Environmental Modeling. *Sensors* **2015**, *15*, 27493–27524. [CrossRef]
6. Deliry, S.I.; Avdan, U. Accuracy of Unmanned Aerial Systems Photogrammetry and Structure from Motion in Surveying and Mapping: A Review. *J. Indian Soc. Remote Sens.* **2021**, *49*, 1997–2017. [CrossRef]
7. Gabrlik, P. The Use of Direct Georeferencing in Aerial Photogrammetry with Micro UAV. *IFAC-Pap.* **2015**, *48*, 380–385. [CrossRef]
8. Grayson, B.; Penna, N.T.; Mills, J.P.; Grant, D.S. GPS Precise Point Positioning for UAV Photogrammetry. *Photogramm. Rec.* **2018**, *33*, 427–447. [CrossRef]
9. Jemai, M.; Loghmari, M.A.; Naceur, M.S. A GNSS Measurement Study Based on RTK and PPK Methods. In Proceedings of the 2023 IEEE International Conference on Advanced Systems and Emergent Technologies (IC_ASET), Hammamet, Tunisia, 29 April–1 May 2023; pp. 1–6.
10. Famiglietti, N.A.; Cecere, G.; Grasso, C.; Memmolo, A.; Vicari, A. A Test on the Potential of a Low Cost Unmanned Aerial Vehicle RTK/PPK Solution for Precision Positioning. *Sensors* **2021**, *21*, 3882. [CrossRef]
11. Alkan, R.M.; Erol, S.; Mutlu, B. Applicability of Real-Time PPP Technique in Polar Regions as an Accurate and Efficient Real-Time Positioning System. *Turk. J. Earth Sci.* **2023**, *32*, 1022–1040. [CrossRef]
12. Xiang, Y.; Gao, Y.; Li, Y. Reducing Convergence Time of Precise Point Positioning with Ionospheric Constraints and Receiver Differential Code Bias Modeling. *J. Geod.* **2020**, *94*, 8. [CrossRef]
13. Calais, E.; Han, J.Y.; DeMets, C.; Nocquet, J.M. Deformation of the North American Plate Interior from a Decade of Continuous GPS Measurements. *J. Geophys. Res. Solid Earth* **2006**, *111*. [CrossRef]
14. Banville, S.; Hassen, E.; Lamothe, P.; Farinaccio, J.; Donahue, B.; Mireault, Y.; Goudarzi, M.A.; Collins, P.; Ghoddousi-Fard, R.; Kamali, O. Enabling Ambiguity Resolution in CSRS-PPP. *NAVIGATION J. Inst. Navig.* **2021**, *68*, 433–451. [CrossRef]
15. Ocalan, T.; Turk, T.; Tunalioglu, N.; Gurturk, M. Investigation of Accuracy of PPP and PPP-AR Methods for Direct Georeferencing in UAV Photogrammetry. *Earth Sci. Inform.* **2022**, *15*, 2231–2238. [CrossRef]
16. Seo, D.-M.; Woo, H.-J.; Hong, W.-H.; Seo, H.; Na, W.-J. Optimization of Number of GCPs and Placement Strategy for UAV-Based Orthophoto Production. *Appl. Sci.* **2024**, *14*, 3163. [CrossRef]
17. Zhao, H.; Li, G.; Chen, Z.; Zhang, S.; Zhang, B.; Cheng, X. Impacts of GCP Distributions on UAV-PPK Photogrammetry at Sermeq Avannarleq Glacier, Greenland. *Remote Sens.* **2024**, *16*, 3934. [CrossRef]
18. Cho, J.M.; Lee, B.K. GCP and PPK Utilization Plan to Deal with RTK Signal Interruption in RTK-UAV Photogrammetry. *Drones* **2023**, *7*, 265. [CrossRef]
19. Elkhrachy, I. Accuracy Assessment of Low-Cost Unmanned Aerial Vehicle (UAV) Photogrammetry. *Alex. Eng. J.* **2021**, *60*, 5579–5590. [CrossRef]

20. Erol, B.; Turan, E.; Erol, S.; Alper Kuçak, R. Comparative Performance Analysis of Precise Point Positioning Technique in the UAV—Based Mapping. *Measurement* **2024**, *233*, 114768. [CrossRef]
21. Tang, L.; Qiao, G.; Li, B.; Yuan, X.; Ge, H.; Popov, S. GNSS-Supported Direct Georeferencing for UAV Photogrammetry without GCP in Antarctica: A Case Study in Larsemann Hills. *Mar. Geod.* **2024**, *47*, 324–351. [CrossRef]
22. Makineci, H.B.; Bilgen, B.; Bulbul, S. A New Precise Point Positioning with Ambiguity Resolution (PPP-AR) Approach for Ground Control Point Positioning for Photogrammetric Generation with Unmanned Aerial Vehicles. *Drones* **2024**, *8*, 456. [CrossRef]
23. Kim, H.; Hyun, C.-U.; Park, H.-D.; Cha, J. Image Mapping Accuracy Evaluation Using UAV with Standalone, Differential (RTK), and PPP GNSS Positioning Techniques in an Abandoned Mine Site. *Sensors* **2023**, *23*, 5858. [CrossRef] [PubMed]
24. Martínez-Carricondo, P.; Agüera-Vega, F.; Carvajal-Ramírez, F. Accuracy Assessment of RTK/PPK UAV-Photogrammetry Projects Using Differential Corrections from Multiple GNSS Fixed Base Stations. *Geocarto Int.* **2023**, *38*, 2197507. [CrossRef]
25. Berber, M.; Munjy, R.; Lopez, J. Kinematic GNSS Positioning Results Compared against Agisoft Metashape and Pix4dmapper Results Produced in the San Joaquin Experimental Range in Fresno County, California. *J. Geod. Sci.* **2021**, *11*, 48–57. [CrossRef]
26. Gurturk, M.; Soycan, M. Accuracy Assessment of Kinematic PPP versus PPK for GNSS Flights Data Processing. *Surv. Rev.* **2022**, *54*, 48–56. [CrossRef]
27. Štroner, M.; Urban, R.; Seidl, J.; Reindl, T.; Brouček, J. Photogrammetry Using UAV-Mounted GNSS RTK: Georeferencing Strategies without GCPs. *Remote Sens.* **2021**, *13*, 1336. [CrossRef]
28. Liu, X.; Lian, X.; Yang, W.; Wang, F.; Han, Y.; Zhang, Y. Accuracy Assessment of a UAV Direct Georeferencing Method and Impact of the Configuration of Ground Control Points. *Drones* **2022**, *6*, 30. [CrossRef]
29. Dönmez, Ş.Ö.; Tunc, A. Transformation methods for using combination of remotely sensed data and cadastral maps. *Int. Arch. Photogramm. Remote Sens. Spat. Inf. Sci.* **2016**, *XLI-B4*, 587–589. [CrossRef]
30. Cevik, I.C.; Atik, M.E.; Duran, Z. Investigation of Optimal Ground Control Point Distribution for Geometric Correction of VHR Remote Sensing Imagery. *J. Indian Soc. Remote Sens.* **2024**, *52*, 359–369. [CrossRef]
31. Guang, Y.; Weili, J. Research on Impact of Ground Control Point Distribution on Image Geometric Rectification Based on Voronoi Diagram. *Procedia Environ. Sci.* **2011**, *11*, 365–371. [CrossRef]
32. Bozkurt, S.; Atik, M.E.; Duran, Z. Improving Aerial Targeting Precision: A Study on Point Cloud Semantic Segmentation with Advanced Deep Learning Algorithms. *Drones* **2024**, *8*, 376. [CrossRef]
33. Lowe, D.G. Distinctive Image Features from Scale-Invariant Keypoints. *Int. J. Comput. Vis.* **2004**, *60*, 91–110. [CrossRef]
34. Atik, M.E.; Ozturk, O.; Duran, Z.; Seker, D.Z. An Automatic Image Matching Algorithm Based on Thin Plate Splines. *Earth Sci. Inform.* **2020**, *13*, 869–882. [CrossRef]
35. Chen, K.; Reichard, G.; Akanmu, A.; Xu, X. Geo-Registering UAV-Captured Close-Range Images to GIS-Based Spatial Model for Building Façade Inspections. *Autom. Constr.* **2021**, *122*, 103503. [CrossRef]
36. Zhao, S.; Kang, F.; Li, J.; Ma, C. Structural Health Monitoring and Inspection of Dams Based on UAV Photogrammetry with Image 3D Reconstruction. *Autom. Constr.* **2021**, *130*, 103832. [CrossRef]
37. Anderle, R.J. Point Positioning Concept Using Precise Ephemeris. *Satell. Doppler Position* **1976**, *1*, 47–75.
38. Zumberge, J.F.; Heflin, M.B.; Jefferson, D.C.; Watkins, M.M.; Webb, F.H. Precise Point Positioning for the Efficient and Robust Analysis of GPS Data from Large Networks. *J. Geophys. Res.* **1997**, *102*, 5005–5017. [CrossRef]
39. Guo, J.; Li, X.; Li, Z.; Hu, L.; Yang, G.; Zhao, C.; Fairbairn, D.; Watson, D.; Ge, M. Multi-GNSS Precise Point Positioning for Precision Agriculture. *Precis. Agric.* **2018**, *19*, 895–911. [CrossRef]
40. Kouba, J. Measuring Seismic Waves Induced by Large Earthquakes with GPS. *Stud. Geophys. Geod.* **2003**, *47*, 741–755. [CrossRef]
41. Xu, P.; Shi, C.; Fang, R.; Liu, J.; Niu, X.; Zhang, Q.; Yanagidani, T. High-Rate Precise Point Positioning (PPP) to Measure Seismic Wave Motions: An Experimental Comparison of GPS PPP with Inertial Measurement Units. *J. Geod.* **2013**, *87*, 361–372. [CrossRef]
42. Jin, S.; Su, K. Co-Seismic Displacement and Waveforms of the 2018 Alaska Earthquake from High-Rate GPS PPP Velocity Estimation. *J. Geod.* **2019**, *93*, 1559–1569. [CrossRef]
43. Oku Topal, G.; Karabulut, M.F.; Aykut, N.O.; Akpınar, B. Performance of Low-Cost GNSS Equipment in Monitoring of Horizontal Displacements. *Surv. Rev.* **2023**, *55*, 536–545. [CrossRef]
44. Yu, C.; Penna, N.T.; Li, Z. Generation of Real-Time Mode High-Resolution Water Vapor Fields from GPS Observations. *J. Geophys. Res. Atmos.* **2017**, *122*, 2008–2025. [CrossRef]
45. Alkan, R.M.; Selbesoğlu, M.O.; Yavaşoğlu, H.H.; Arkalı, M. Seamless precise kinematic positioning in the high-latitude environments: Case study in the antarctic region. *Rud. Geol. Naft. Zb.* **2024**, *39*, 31–43. [CrossRef]
46. Leick, A.; Rapoport, L.; Tatarnikov, D. *GPS Satellite Surveying*; John Wiley & Sons: Hoboken, NJ, USA, 2015; ISBN 978-1-118-67557-1.
47. Xiao, G.; Yang, C.; Wei, H.; Xiao, Z.; Zhou, P.; Li, P.; Dai, Q.; Zhang, B.; Yu, C. PPP Ambiguity Resolution Based on Factor Graph Optimization. *GPS Solut.* **2024**, *28*, 178. [CrossRef]
48. Hatch, R. The Synergism of GPS Code and Carrier Measurements. *Int. Geod. Symp. Satell. Doppler Position.* **1983**, *2*, 1213–1231.
49. Melbourne, W.G. The Case for Ranging in GPS-Based Geodetic Systems. In Proceedings of the First International Symposium on Precise Positioning with the Global Positioning System, Rockville, MD, USA, 15–19 April 1985; pp. 373–386.

50. Wübbena, G. Software Developments for Geodetic Positioning with GPS Using TI-4100 Code and Carrier Measurements. In Proceedings of the First International Symposium on Precise Positioning with the Global Positioning System, Rockville, MD, USA, 15–19 April 1985; Volume 19, pp. 403–412.
51. Aykut, N.O.; Gülal, E.; Akpinar, B. Performance of Single Base RTK GNSS Method versus Network RTK. *Earth Sci. Res. J.* **2015**, *19*, 135–139. [CrossRef]
52. AtiZ, Ö.F.; Konukseven, C.; Öğütcü, S.; Alçay, S. Comparative Analysis of the Performance of Multi-GNSS RTK: A Case Study in Turkey. *Int. J. Eng. Geosci.* **2022**, *7*, 67–80. [CrossRef]
53. Taddia, Y.; Stecchi, F.; Pellegrinelli, A. Coastal Mapping Using DJI Phantom 4 RTK in Post-Processing Kinematic Mode. *Drones* **2020**, *4*, 9. [CrossRef]
54. Specs—DJI Mavic 3 Enterprise—DJI Enterprise. Available online: https://enterprise.dji.com/mavic-3-enterprise (accessed on 24 December 2024).
55. İSKİ Uydulardan Konum Belirleme Sistemi—UKBS Nedir? Available online: https://ukbs.iski.gov.tr/icerik/ukbs-nedir (accessed on 30 November 2024).
56. REDtoolbox—PPK and Geotagging. Available online: https://www.redcatch.at/redtoolbox/ (accessed on 20 December 2024).
57. Geng, J.; Chen, X.; Pan, Y.; Mao, S.; Li, C.; Zhou, J.; Zhang, K. PRIDE PPP-AR: An Open-Source Software for GPS PPP Ambiguity Resolution. *GPS Solut.* **2019**, *23*, 91. [CrossRef]
58. Vázquez-Ontiveros, J.R.; Padilla-Velazco, J.; Gaxiola-Camacho, J.R.; Vázquez-Becerra, G.E. Evaluation and Analysis of the Accuracy of Open-Source Software and Online Services for PPP Processing in Static Mode. *Remote Sens.* **2023**, *15*, 2034. [CrossRef]